Arabian Journal of Chemistry (2020) 13, 8301–8308

King Saud University

Arabian Journal of Chemistry

www.ksu.edu.sa
www.sciencedirect.com

ORIGINAL ARTICLE

Selective synthesis of ZIFs from zinc and nickel nitrate solution for photocatalytic H_2O_2 production

Ai-Lun Chang [a], Van-Huy Nguyen [b], Kun-Yi Andrew Lin [c], Chechia Hu [a,*]

[a] *Department of Chemical Engineering, R&D Center for Membrane Technology and Research Center for Circular Economy, Chung Yuan Christian University, Chungli Dist., Taoyuan City 32023, Taiwan*
[b] *Institute of Research and Development, Duy Tan University, Da Nang 550000, Viet Nam*
[c] *Department of Environmental Engineering & Innovation and Development Center of Sustainable Agriculture, National Chung Hsing University, Taichung City 40227, Taiwan*

Received 21 February 2020; accepted 22 April 2020
Available online 29 April 2020

KEYWORDS

Zinc nitrate;
Nickel nitrate;
ZIF-8;
ZIF-L;
Photocatalysis;
H_2O_2 production

Abstract Hydrogen peroxide (H_2O_2) is one of the most promising, green, and effective oxidants that can be used in different applications. In this study, zeolitic imidazolate frameworks (ZIFs), consisting of organic ligands and metal sites, were selectively prepared from zinc or nickel nitrate solutions for use in photocatalytic H_2O_2 production. High concentrations of zinc nitrate solution provided more metal sites to coordinate with 2-methylimidazole, producing ZIF-8 with larger particle size, whereas low zinc nitrate concentrations resulted in more interconnected N–H···N hydrogen bonds, forming 2D-layered ZIF-L, with smaller particle size. Various concentrations of zinc and nickel nitrate solutions produced ZIFs that exhibited ZIF-8 or ZIF-L topology, with bandgap energies of 5.45 and 4.85 eV, respectively. These samples could serve as promising photocatalyst for the successful production of H_2O_2 under Xenon lamp irradiation.

1. Introduction

In recent decades, hydrogen peroxide (H_2O_2) has been widely used as an eco-friendly oxidant in many applications. Because of its high energy density, it can serve as an alternative liquid fuel, with the advantage that it generates only water and oxygen after use (Hirakawa et al., 2016; Li et al., 2016). H_2O_2 is produced industrially by the anthraquinone method, which is a high-cost process (Yang et al., 2018). Given the urgent demand for H_2O_2, the photocatalytic or electrocatalytic production of H_2O_2 from oxygen reduction or water oxidation reaction is becoming attractive as a potential clean alternative. The production of H_2O_2 from an oxygen reduction reaction generally involves a two-electron transfer according to the equation below (Yang et al., 2017):

$$O_2 + 2H^+ + 2e^- \rightarrow H_2O_2 \ (E = 0.68 \text{ V vs NHE, pH} = 0)$$

In addition, H_2O_2 production from water oxidation requires a large overpotential (~1.8 V), which is difficult to

* Corresponding author.
E-mail address: chechiahu@cycu.edu.tw (C. Hu).
Peer review under responsibility of King Saud University.

Production and hosting by Elsevier

https://doi.org/10.1016/j.arabjc.2020.04.027
1878-5352

achieve through photocatalysis or electrocatalysis. Therefore, many researchers have produced H_2O_2 in water or various alcohol/water mixtures by continuously purging O_2 through photocatalysis under light irradiation. In this scenario, appropriate selection of the photocatalyst could be one of the most important factors to improve the adsorption of the reactant molecules (Agarwal et al., 2016; Fakhri et al., 2016; Fakhri, 2017; Gupta et al., 2016, 2017a, 2017b, 2017c), surface reaction (Zaid et al., 2015; Ammar et al., 2016; Sharma et al., 2016; Tiwari et al., 2017), and the catalytic production of H_2O_2.

Zeolitic imidazolate frameworks (ZIFs) have attracted significant attention because of their outstanding physical and chemical properties, such as high specific surface areas, high crystallinities, surface functionalities, and chemical/thermal stabilities (Lee et al., 2015; Lo et al., 2016; Zanon and Verpoort, 2017; Vega et al., 2019). Most importantly, ZIFs, which consist of metal sites linked with surrounding organic ligands, can be easily tailored and functionalized to serve as adsorption sites, catalytic centers, or photocatalytic centers (Wu et al., 2015; Gao et al., 2018; Lin et al., 2018; Isaka et al., 2019; Chen et al., 2020; Huang et al., 2020). Hamad et al. suggested that the structures of ZIFs with a single type of organic linker exhibit wide band gaps; however, by grafting other linkers or introducing metal, such as copper, could increase the photo-absorption and prolong the lifetime of the photoexcited electron-hole pairs (Grau-Crespo et al., 2016). Among the various ZIFs, ZIF-8, which contains Zn^{2+} tetrahedrally-coordinated with imidazolate groups, has high chemical and thermal stability, a large specific surface area, and high porosity, which facilitate its use in gas separation, CO_2 adsorption, heterogeneous and catalysis (Yang et al., 2015; Jian et al., 2015; Hu et al., 2019; Oh et al., 2020). The theoretically calculated band gap energy of ZIF-8 is approximately 5 eV, which can straddle the reduction and oxidation potentials of water for photocatalysis (Grau-Crespo et al., 2016). In addition, ZIF-8 has high water stability, making it a good candidate for a heterogeneous catalyst. On the other hand, ZIF-L, with the same building blocks as ZIF-8, is a two-dimensional layered metal-organic framework (MOF). The ZIF-L layers are stacked along the *c*-axis between 2-methylimidazole units to yield a cushion-type structure. Pan and his coworkers have compared the pervaporation performance of ZIF-8 and ZIF-L as hybrid membranes (Liu et al., 2017). The ZIF-L membrane shows superior separation performance because of its ordered alignment, which allows for rapid transport of water molecules, as well as its high resistance to swelling and excellent thermal and mechanical stabilities. ZIF-8 and ZIF-L have considerable similarity in their structures. ZIF-L, with a two-dimensional structure, is a metastable phase and can be converted to ZIF-8 by changing the metal (zinc) salt, the 2-methylimidazole (Hmim) linker, or the solvent. Zhang et al. have shown that when cobalt is used as the metal center, the Co/Hmim ratio plays an important role: a higher ratio promotes the crystallization of ZIF-L-Co (Zhang et al., 2015). Wang et al. reported that a fast phase transformation from irregular ZIF-L to ZIF-8 could be achieved by treatment with polyvinylpyrrolidone (PVP) and ethanol (Fu et al., 2018). Most importantly, in the past decade, approximately 250 papers have been published, with rapid growth in the number of citations: a citation search of the Web of Science using the keywords

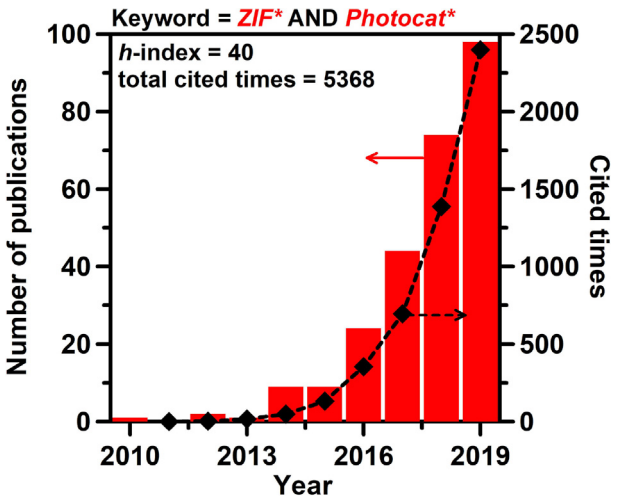

Fig. 1 Number of publications and times cited against year, searched by keywords "ZIF*" and "Photocat*" using the *Web of Science* on February 3rd 2020.

"ZIF*" and "Photocat*" produced 5300 cited times (Fig. 1). The *h*-index of 40 for photocatalytic reactions using ZIFs also shows that this topic is of particular interest to researchers worldwide. However, to the best of our knowledge, there are no reports on the selective synthesis and structure and morphology control of ZIFs by changing the precursors, or on the determination of the photocatalytic activity for the production of H_2O_2.

In this study, ZIF-8 and ZIF-L were prepared for photocatalytic H_2O_2 production by using $Ni(NO_3)_2$ and $Zn(NO_3)_2$ as precursors with Hmim in deionized water solution. The crystal structure, optical absorption, surface functional groups, morphology, and appearance of the products were investigated. The phase transformation from ZIF-L to ZIF-8 was also observed. Our results suggest that the phase transition between ZIF-8 and ZIF-L can be easily controlled by using different metal nitrate solutions as precursors. In this work, we report a new finding that ZIF-8 and ZIF-L can serve as photocatalysts for H_2O_2 production, and discuss the phase transformation from controlling the precursors of ZIFs.

2. Experimental

2.1. Synthesis of ZIFs

For the synthesis of ZIF-8, a solution of 2-methylimidazole (Hmim, 8.2 g in 20 mL water) and a solution of zinc nitrate hexahydrate (1.894 g in 10 mL water) were mixed in a mole ratio of 10:1 and stirred for at least 10 min for homogeneous mixing. Then, the solution was heated to 40 °C for 30 min and centrifuged at 9000 rpm for 5 min, yielding a precipitate. The precipitate was collected, washed with methanol several times, and dried at 60 °C for 24 h to yield ZIF-8. The procedure for the synthesis of ZIF-L was identical to that mentioned above, except that the zinc nitrate solution was replaced by a nickel nitrate solution (1.83 g in 10 mL water). The use of a mixture of zinc nitrate (0.947 g in 10 mL water) and nickel nitrate solutions (0.914 g in 10 mL water) in a mole ratio of

1:1 produced ZnNi-ZIF. All chemicals were purchased from Sigma-Aldrich and used without purification.

2.2. Characterizations

The crystal structures of the samples were determined by X-ray diffraction (Bruker D8 advance, USA), using Cu Kα radiation (λ = 1.5406 Å) at 2θ angles of 5°–50° and a scan rate of 4° min^{-1}. Fourier transform infrared spectroscopy (FTIR; Tensor 27, Bruker, USA) was employed to investigate the functional groups and chemical states of the specimens. The microstructures and appearance of the samples were examined by scanning electron microscopy (SEM; Hitachi S-4800N, Japan). The particle sizes of the samples were investigated by dynamic light scattering technique (DLS) using a size analyzer (Beckman Coulter, DelsaNano S). The ultraviolet–visible light absorption properties of the samples were measured using an ultraviolet–visible (UV–Vis; Hitachi U-3900, Japan) spectrometer. The band gap energy was determined from a Tauc plot, wherein the curve of $(\alpha h\nu)^{1/r}$ against $h\nu$ (where α is the absorption coefficient of the material, $h\nu$ is the photon energy, and r = 1/2 for direct, 2 for indirect transitions) was extrapolated to intersect the energy axis.

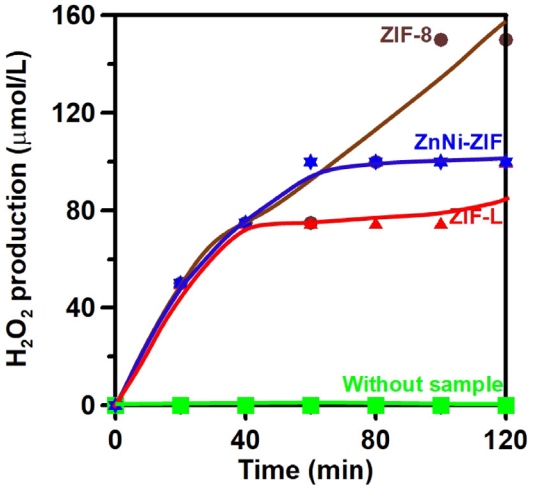

Fig. 2 Photocatalytic H_2O_2 production using ZIF-8, ZnNi-ZIF, and ZIF-L, with continuous O_2 purge in aqueous solution under Xenon lamp irradiation.

2.3. Photocatalytic reaction

For the photocatalytic H_2O_2 production, the photocatalyst powders (0.05 g) were suspended and stirred in 100 mL of aqueous deionized water, with a continuous flow of O_2 through the suspension at a rate of 50 mL min^{-1}. A 350 W Xenon lamp was used as the light source without a cutoff filter. The H_2O_2 produced was measured by GC-FID (GC-2014, Shimadzu, Japan) and by a titration method. In the latter case, sulfuric acid was added to the solution, followed by titration using $KMnO_4$ solution; the endpoint was indicated by a light red color maintained for at least 30 s. Each titration was repeated at least three times.

3. Results and discussion

3.1. Photocatalytic H_2O_2 production

Fig. 2 shows photocatalytic H_2O_2 production plotted against time, using ZIF-8, ZIF-L, and ZnNi-ZIF samples, under irradiation by a Xenon lamp and continuous purging with O_2 gas. It can be seen that the activity of ZIF-8 in the generation of H_2O_2 is higher than that of ZIF-L and ZnNi-ZIF and that H_2O_2 production using ZIF-L reached a constant value after 40 min. On the other hand, no H_2O_2 can be detected without the addition of the samples, indicating that H_2O_2 production is

Table 1 Photocatalytic H_2O_2 production using different photocatalysts as reported in previous studies.

H_2O_2 (μmol/L-h)	Sample	Lamp	Solutions	Ref.
~ 9.5	Cv-g-C_3N_4 (0.02 g)	Xenon lamp (> 420 nm)	Ethanol/Water (9/1), 5 mL	Shiraishi et al. (2015)
~ 210	C-modified g-C_3N_4 (0.03 g)	300 W Xenon lamp (> 420 nm)	Water, 30 mL containing IPA (5 vol%)	Wang et al. (2018)
~2.4	Defective g-C_3N_4 (0.05 g)	AM1.5 (> 420 nm)	Water, 60 mL containing IPA (20 vol%)	Shi et al. (2018)
~140	Ti_3C_2/g-C_3N_4 (0.05 g)	300 W Xenon lamp (> 420 nm)	Water, 50 mL containing IPA (10 vol%)	Yang et al. (2019)
~1150	$FeVO_4$/CF cathode-ZnO/Zn anode	36 W UV lamp	NaCl solution (500 or 10 mmol/L)	Xu et al. (2019)
~25	g-C_3N_4 (0.03 g)	300 W iodine tungsten lamp (> 420 nm)	Water, 60 mL	Lu et al. (2020)
~50	ZnO (0.2 g)	300 W Xenon lamp	Water, 100 mL containing NaF (0,1 M) and ethanol (4%)	Meng et al. (2020)
~1525	0.1%Au/ZnO (0.2 g)	300 W Xenon lamp	Water, 100 mL containing NaF (0,1 M) and ethanol (4%)	Meng et al. (2020)
~75	ZIF-8 (0.05 g)	350 W Xenon lamp	Water, 100 mL	This work
~50	ZIF-L (0.05 g)	350 W Xenon lamp	Water, 100 mL	This work

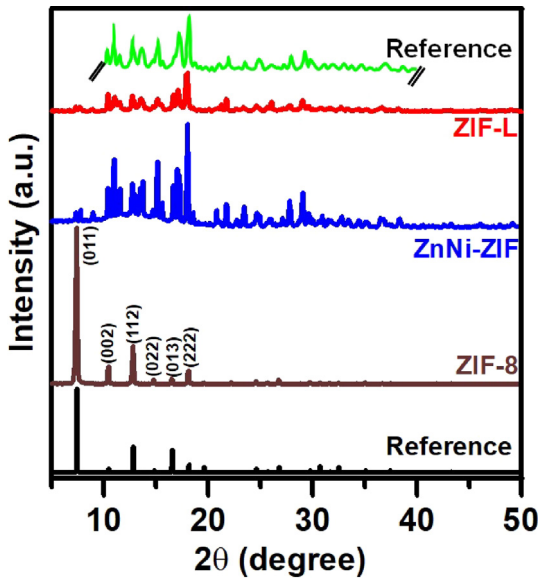

Fig. 3 XRD patterns of ZIF-8, ZnNi-ZIF, ZIF-L, and the comparative data obtained from previous studies (Hu et al., 2019; Park et al., 2006; Chen et al., 2013; Nasir et al., 2018).

mainly due to photocatalysis triggered by ZIF-8, ZIF-L, or ZnNi-ZIF. The total H_2O_2 concentrations produced within 2 h using ZIF-8, ZnNi-ZIF, and ZIF-L were approximately 0.15, 0.1, and 0.1 mmol/L, respectively. However, the ZnNi-ZIF sample deactivated quickly after irradiation for 1 h. Compared to the values reported in previous studies, the H_2O_2 production activity using ZIF-8 or ZIF-L is similar to that of other catalysts in the presence of pure water (Table 1) but much lower than that with the addition of scavengers. Nevertheless, our samples still show promise as functional photocatalysts for the production of H_2O_2 under light irradiation.

3.2. Crystalline structure of ZIFs

The crystal structures of ZIF-8, ZnNi-ZIF, and ZIF-L were determined by XRD, as shown in Fig. 3. The main peaks of ZIF-8 were found at approximately 7.3°, 10.4°, 12.7°, 14.7°, 16.4°, and 18.0°, which refer to the crystallographic planes (0 1 1), (0 0 2), (1 1 2), (0 2 2), (0 1 3), and (2 2 2), respectively, and these peaks are consistent with those reported in previous studies (Park et al., 2006; Yang et al., 2015). The XRD patterns of ZIF-L and ZnNi-ZIF exhibited prominent peaks at 2θ values between 10° and 20°, which were identical to the previously reported peaks (Chen et al., 2013; Nasir et al., 2018). These characteristic peaks showed that the ZIF-L and ZnNi-ZIF have similar crystal structures, with a two-dimensional framework containing one large zero-dimensional cavity within the layers, and an orthorhombic unit cell (a = 24.06 Å, b = 16.97 Å, c = 19.68 Å) typical of a semi-sodalite structure.

Fig. 4 shows a schematic illustration of the structures of ZIF-8 and ZIF-L. It has been reported that the phase transformation of ZIF-L and ZIF-8 can be carefully controlled by a post-washing process using various solvents, or by the addition of PVP to facilitate the nucleation of ZIF-L (Fu et al., 2018). Wang et al. also suggested that the interaction between Zn^{2+} and N atoms in the solvent enables better control of the crystallinity and particle size of ZIF-L and ZIF-8 (Fu et al., 2018). Note that although ZIF-8 and ZIF-L both consist of the same building blocks of metal clusters connected with Hmim, as shown in Fig. 4, ZIF-L is bridged by N–H···N hydrogen bonds to form a 2D-layered network, whereas ZIF-8 has a sodalite topology with strong coordination of Zn^{2+} with the surrounding N–H bonds. This indicates that the transformation between ZIF-8 and ZIF-L could result in a structural distortion. We, therefore, employed the Williamson-Hall (W-H) equation, $\beta_{hkl}\cos\theta = (K\lambda/D_{W\text{-}H}) + 4\varepsilon\sin\theta$ (Zak et al., 2011; Yang et al., 2020) to determine the lattice strain, based on a uniform deformation model. In this equation, β_{hkl} refers to the peak width at the half-maximum intensity of the reflection from the (hkl) plane, K is a constant, λ is the wavelength of the incident X-rays, $D_{W\text{-}H}$ is the crystallite size, and ε is the lattice strain from crystal imperfection and distortion. Fig. 5 shows a plot of $4\sin\theta$ against $\beta_{hkl}\cos\theta$, from which ε and $D_{W\text{-}H}$ are obtained from the slope and intercept. The negative ε values for the samples indicate that the lattice shrank slightly along the crystallographic axes. ZnNi-ZIF has a more negative ε value, implying it has greater lattice strain and more crystal imperfections than ZIF-L and ZIF-8 have.

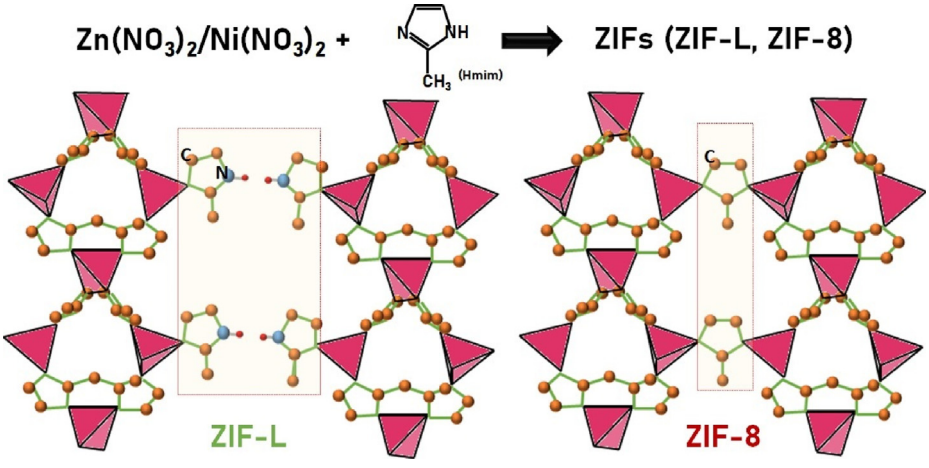

Fig. 4 Schematic illustration of the crystal structures of ZIF-8 and ZIF-L.

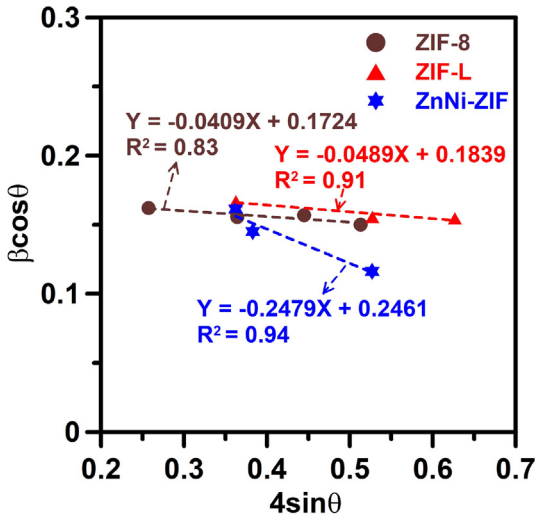

Fig. 5 Williamson-Hall plot for ZIF-8, ZnNi-ZIF, and ZIF-L samples. The lines shown are the linear regression lines to the data for the corresponding samples.

3.3. Morphologies of ZIFs

Fig. 6 shows the SEM images of the ZIF-8, ZnNi-ZIF, and ZIF-L samples. Interestingly, ZIF-8 has a much larger particle size (approximately 1 to a few μm) than that of ZIF-L (approximately 20 to 80 nm). Crystallites of ZIF-8 exhibit shapes with pseudo-cubic and rod-like configurations; those of ZIF-L have an irregular-circular shape; and ZnNi-ZIF shows a cushion-connected structure that is similar to that previously reported (Liu et al., 2017). The structural change can be attributed to the fact that high concentrations of $Zn(NO_3)_2$ relative to Hmim in water can facilitate the nucleation of ZIF-8, whereas a low ratio could more easily generate ZIF-L (Fu et al., 2018). In our case, the relatively low concentration of $Zn(NO_3)_2$ indicates a lack of metal sites to graft Hmim, resulting in interconnection by N–H···N hydrogen bonds in water as a solvent. Besides, we also prepared *x*Ni-ZIF-8 with different zinc to nickel ratio for comparison (detailed synthesis was shown in Supporting Information). The DLS analysis and SEM images in Fig. S1 suggested that particle sizes of *x*Ni-ZIF-8 became larger than that of ZIF-8, agreeing with the SEM observation in Fig. 6. On the other hand, heat treatment of the mixture of $Zn(NO_3)_2$ and Hmim is beneficial for crystal growth and nucleation, producing particles with a larger size than those of ZIF-L.

3.4. FTIR and UV–vis spectra of ZIFs

FTIR was employed to investigate the surface functional groups of the ZIF-8, ZnNi-ZIF, and ZIF-L samples in Fig. 7. Interestingly, the FTIR spectra of these samples were identical in the range 3200–3600 cm^{-1}, containing peaks that represent symmetric and asymmetric vibrations of the N-H groups (Zhang et al., 2019). The peaks in the regions 900–1350 cm^{-1} and 1350–1500 cm^{-1} can be attributed to the in-plane bending and stretching modes of vibration of the imidazole ring of ZIF-8 (Gadipelli et al., 2014), and the bands at 1640 and 1148 cm^{-1} were assigned to C═N and C─N

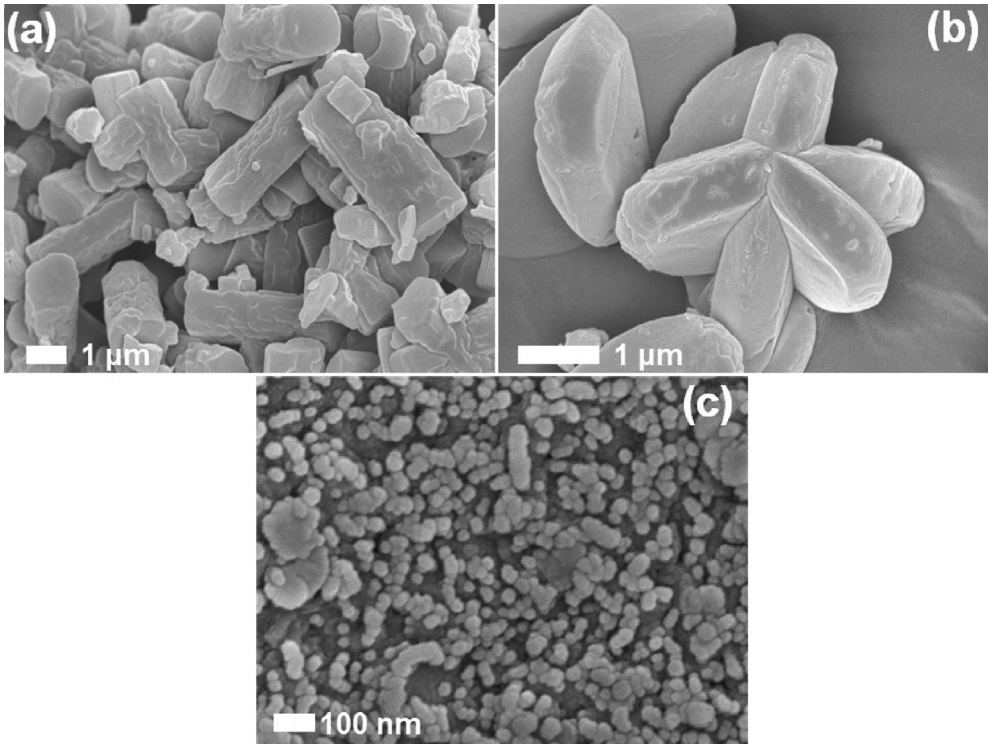

Fig. 6 SEM images of (a) ZIF-8, (b) ZnNi-ZIF, and (c) ZIF-L samples.

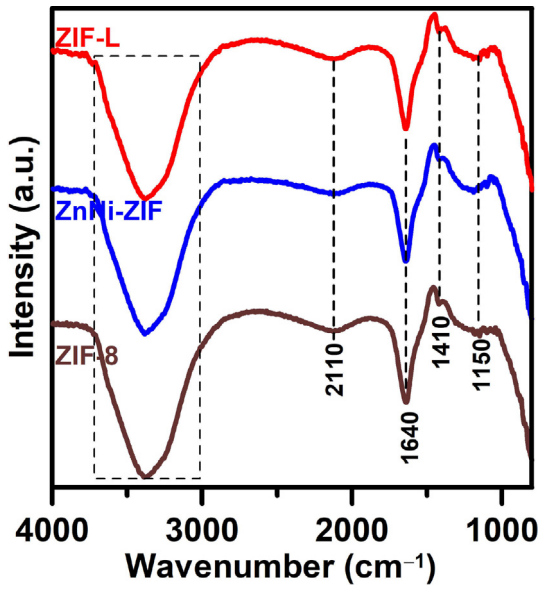

Fig. 7 FTIR spectra of ZIF-8, ZnNi-ZIF, and ZIF-L samples.

stretching, respectively (Wu et al., 2017). The interlayered functional groups of ZIF-8 and ZIF-L are difficult to detect, but these samples have similar surface functional groups, resulting in their similar FTIR spectra.

The UV–vis absorbance spectra of ZIF-8, ZnNi-ZIF, and ZIF-L in Fig. 8 show that ZIF-8, ZnNi-ZIF, and ZIF-L have an absorption edge at approximately 240, 268, and 270 nm, respectively. The spectra of ZIF-8 and ZIF-L are consistent with those previously reported (Hu et al., 2019). The band gap energy of these samples can be easily obtained by calculating the intercept of the Tauc plot (as shown in the inset of Fig. 8). ZIF-8 has a larger band gap energy (5.45 eV) than that of ZIF-L and ZnNi-ZIF (4.85 eV), these values indicating that transitions in both samples could only be triggered by ultraviolet light, and the energy band position of ZIF-8 could hurdle the redox potential for H_2O_2 production and water splitting as shown in the inset of Fig. 8 (Grau-Crespo et al., 2016). The larger band gap energy of ZIF-8 may result in less charge recombination (Butler et al., 2017; Chin et al., 2018), and hence higher photocatalytic activity under Xenon lamp irradiation. The photoexcited electrons and holes of the photocatalyst could react with oxygen and water molecules to generate H_2O_2 and O_2, respectively (Li et al., 2016). But we are unable to detect O_2 production because of our system was open to atmosphere and continuously purging with O_2 during the reaction. Further investigation is still required to determine the mechanism of photocatalysis using ZIFs.

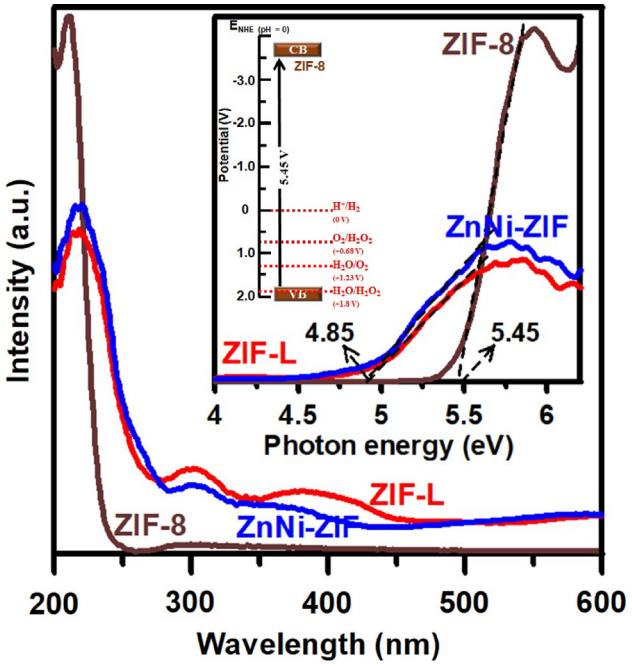

Fig. 8 UV–Vis spectra of ZIF-8, ZnNi-ZIF, and ZIF-L samples. The inset shows the Tauc plot of these samples and the proposed energy potential of ZIF-8.

4. Conclusions

In this study, zinc nitrate and nickel nitrate solution were used as precursors together with 2-methylimidazole, to selectively construct zeolite imidazolate frameworks (ZIFs) for photocatalytic H_2O_2 production. At higher concentrations of the zinc nitrate solution, ZIF-8 was obtained, suggesting that Zn^{2+} sites could coordinate strongly with the surrounding N–H bonds to result in a sodalite topology of ZIF-8. On the other hand, lower concentrations of zinc nitrate let to the formation of ZIF-L, suggesting that fewer Zn^{2+} sites may allow the formation of N–H···N hydrogen bonds, producing the 2D-layered structure of ZIF-L. Moreover, higher concentrations of the zinc nitrate solution could result in a higher nucleation rate, thereby producing larger particles of ZIF-8. We have concluded that ZIF-8 has a larger particle size and wider band gap energy than those of ZIF-L, leading to higher activity for photocatalytic H_2O_2 production. We have also demonstrated a simple, feasible, and rational design to derive zeolite imidazolate frameworks, using different metal nitrate concentrations to selectively produce either ZIF-8 or ZIF-L. ZIFs can serve as potential light-induced catalysts for photocatalytic H_2O_2 production.

Declaration of Competing Interest

The authors declared no potential conflicts of interest with respect to the research, authorship, and/or publication of this article.

Acknowledgement

This research was supported by the Ministry of Science and Technology, Taiwan (107-2221-E-033-032-MY3, 108-2221-E-033-034-MY3). We are also grateful to receive funding from Chung Yuan Christian University for the International Collaboration Program.

Appendix A. Supplementary material

Supplementary data to this article can be found online at https://doi.org/10.1016/j.arabjc.2020.04.027.

References

Agarwal, S., Sadeghi, N., Tyagi, I., Gupta, V.K., Fakhri, A., 2016. Adsorption of toxic carbamate pesticide oxamyl from liquid phase by newly synthesized and characterized graphene quantum dots nanomaterials. J. Colloid. Interf. Sci. 215, 269–275. https://doi.org/10.1016/j.molliq.2015.12.033.

Ammar, A., Al-Enizi, A.M., AlMaadeed, M.A., Karim, A., 2016. Influence of graphene oxide on mechanical, morphological, barrier, and electrical properties of polymer membranes. Arab. J. Chem. 9, 274–286. https://doi.org/10.1016/j.arabjc.2015.07.006.

Butler, K.T., Hendon, C.H., Walsh, A., 2017. Designing porous electronic thin-film devices: band offsets and heteroepitaxy. Farad. Discussion 201, 207–219. https://doi.org/10.1039/C7FD00019G.

Chen, R., Yao, J., Gu, Q., Smeets, S., Baerlocher, C., Gu, H., Zhu, D., Morris, W., Yaghi, O.M., Wang, H., 2013. A two-dimensional zeolitic imidazolate framework with a cushion-shaped cavity for CO_2 adsorption. Chem. Commun. 49, 9500–9502. https://doi.org/10.1039/C3CC44342F.

Chin, M., Cisneros, C., Araiza, S.M., Vargas, K.M., Ishihara, K.M., Tian, F., 2018. Rhodamine B degradation by nanosized zeolitic imidazolate framework-8 (ZIF-8). RSC Adv. 8, 26987–26997. https://doi.org/10.1039/C8RA03459A.

Chen, X.L., Kuwahara, Y., Mori, K., Louis, C., Yamashita, H., 2020. A hydrophobic titanium doped zirconium-based metal organic framework for photocatalytic hydrogen peroxide production in a two-phase system. J. Mater. Chem. A 8, 1904–1910. https://doi.org/10.1039/c9ta11120d.

Fakhri, A., Rashidi, S., Asif, M., Tyagi, I., Agarwal, S., Gupta, V.K., 2016. Dynamic adsorption behavior and mechanism of Cefotaxime, Cefradine and Cefazolin antibiotics on CdS-MWCNT nanocomposites. J. Mole. Liq. 215, 269–275. https://doi.org/10.1016/j.molliq.2015.12.033.

Fakhri, A., 2017. Adsorption characteristics of graphene oxide as a solid adsorbent for aniline removal from aqueous solutions: Kinetics, thermodynamics and mechanism studies. J. Saudi Chem. Soc. 21, S52–S57. https://doi.org/10.1016/j.jscs.2013.10.002.

Fu, H., Wang, Z., Wang, X., Wang, P., Wang, C.C., 2018. Formation mechanism of rod-like ZIF-L and fast phase transformation from ZIF-L to ZIF-8 with morphology changes controlled by polyvinylpyrrolidone and ethanol. CrystEngComm 20, 1473–1477. https://doi.org/10.1039/C7CE02073B.

Gadipelli, S., Travis, W., Zhou, W., Guo, Z., 2014. A thermally derived and optimized structure from ZIF-8 with giant enhancement in CO_2 uptake. Energ. Environ. Sci. 7, 2232–2238. https://doi.org/10.1039/C4EE01009D.

Gupta, V.K., Agarwal, S., Tyagi, I., Sohrabi, M., Fakhri, A., Rashidi, S., Sadeghi, N., 2016. Microwave-assisted hydrothermal synthesis and adsorption properties of carbon nanofibers for methamphetamine removal from aqueous solution using a response surface methodology. J. Ind. Eng. Chem. 41, 158–164. https://doi.org/10.1016/j.jiec.2016.07.018.

Grau-Crespo, R., Aziz, A., Collins, A.W., Crespo-Otero, R., Hernández, N.C., Rodriguez-Albelo, L.M., Ruiz-Salvador, R., Calero, S., Hamad, S., 2016. Modelling a linker mix-and-match approach for controlling the optical excitation gaps and band alignment of zeolitic imidazolate frameworks. Angew. Chem. Int. Ed. 55, 16012–16016. https://doi.org/10.1002/anie.201609439.

Gupta, V.K., Agarwal, S., Bharti, A.K., Fakhri, A., Naji, M., 2017a. Pt nanoparticles decorated WO_3-MWCNTs nanocomposites: Preparation, characterization, and adsorption behavior. J. Mole. Liq. 229, 514–519. https://doi.org/10.1016/j.molliq.2016.12.102.

Gupta, V.K., Agarwal, S., Asif, M., Fakhri, A., Sadeghi, N., 2017b. Application of response surface methodology to optimize the adsorption performance of a magnetic graphene oxide nanocomposite adsorbent for removal of methadone from the environment. J. Colloid. Interf. Sci. 497, 193–200. https://doi.org/10.1016/j.jcis.2017.03.006.

Gupta, V.K., Fakhri, A., Bharti, A.K., Agarwal, S., Naji, M., 2017c. Optimization by response surface methodology for vanadium (V) removal from aqueous solutions using PdO-MWCNTs nanocomposites. J. Mole. Liq. 234, 117–123. https://doi.org/10.1016/j.molliq.2017.03.061.

Gao, Y., Qiao, Z., Zhao, S., Wang, Z., Wang, J., 2018. In situ synthesis of polymer grafted ZIFs and application in mixed matrix membrane for CO_2 separation. J. Mater. Chem. A 6, 3151–3161. https://doi.org/10.1039/C7TA10322K.

Hirakawa, H., Shiota, S., Shiraishi, Y., Sakamoto, H., Ichikawa, S., Hirai, T., 2016. Au nanoparticles supported on $BiVO_4$: Effective inorganic photocatalysts for H_2O_2 production from water and O_2 under visible light. ACS Catal. 6, 4976–4982. https://doi.org/10.1021/acscatal.6b01187.

Hu, C.C., Huang, Y.C., Chang, A.L., Nomura, M., 2019. Amine functionalized ZIF-8 as a visible-light-driven photocatalyst for Cr (VI) reduction. J. Colloid. Interf. Sci. 553, 372–381. https://doi.org/10.1016/j.jcis.2019.06.040.

Huang, C.C., Nguyen, V.H., Zhou, S.R., Hsu, S.Y., Tan, J.X., Wu, K. C.W., 2020. Metal–organic frameworks: preparation and applications in highly efficient heterogeneous photocatalysis. Sustain. Energ. Fuels 4, 504–521. https://doi.org/10.1039/C9SE00972H.

Isaka, Y., Kawase, Y., Kuwahara, Y., Mori, K., Yamashita, H., 2019. Two-phase system utilizing hydrophobic metal–organic frameworks (MOFs) for photocatalytic synthesis of hydrogen peroxide. Angew. Chem. Int. Ed. 58, 5402–5406. https://doi.org/10.1002/anie.201901961.

Jian, M., Liu, B., Zhang, G., Liu, R., Zhang, X., 2015. Adsorptive removal of arsenic from aqueous solution by zeolitic imidazolate framework-8 (ZIF-8) nanoparticles. Colloid. Surf. A 465, 67–76. https://doi.org/10.1016/j.colsurfa.2014.10.023.

Lee, W.C., Chien, H.T., Lo, Y., Chiu, H.C., Wang, T.P., Kang, D.Y., 2015. Synthesis of zeolitic imidazolate framework core–shell nanosheets using zinc-imidazole pseudopolymorphs. ACS Appl. Mater. Interf. 7, 18353–18361. https://doi.org/10.1021/acsami.5b04217.

Li, S., Dong, G., Hailili, R., Yang, L., Li, Y., Wang, F., Zeng, Y., Wang, C., 2016. Effective photocatalytic H_2O_2 production under visible light irradiation at g-C_3N_4 modulated by carbon vacancies. Appl. Catal. B-Environ. 190, 26–35. https://doi.org/10.1016/j.apcatb.2016.03.004.

Lo, Y., Lam, C.H., Chang, C.W., Yang, A.C., Kang, D.Y., 2016. Polymorphism/pseudopolymorphism of metal–organic frameworks composed of zinc(II) and 2-methylimidazole: synthesis, stability, and application in gas storage. RSC Adv. 6, 89148–89156. https://doi.org/10.1039/C6RA19437K.

Liu, G., Jiang, Z., Cao, K., Nair, S., Cheng, X., Zhao, J., Gomaa, H., Wu, H., Pan, F., 2017. Pervaporation performance comparison of hybrid membranes filled with two-dimensional ZIF-L nanosheets and zero-dimensional ZIF-8 nanoparticles. J. Membr. Sci. 523, 185–196. https://doi.org/10.1016/j.memsci.2016.09.064.

Lin, L., Liu, H., Zhang, X., 2018. Flower-like ZnO-assisted one-pot encapsulation of noble metal nanoparticles supported catalysts with ZIFs. Appl. Surf. Sci. 433, 602–609. https://doi.org/10.1016/j.apsusc.2017.10.047.

Lu, N., Liu, N., Hui, Y., Shang, K., Jiang, N., Li, J., Wu, Y., 2020. Characterization of highly effective plasma-treated g-C_3N_4 and application to the photocatalytic H_2O_2 production. Chemosphere 241,. https://doi.org/10.1016/j.chemosphere.2019.124927 124927.

Meng, X., Zong, P., Wang, L., Yang, F., Hou, W., Zhang, S., Li, B., Guo, Z., Liu, S., Zuo, G., Du, Y., Wang, T., Roy, V.A.L., 2020. Au-nanoparticle-supported ZnO as highly efficient photocatalyst for H_2O_2 production. Catal. Commun. 134,. https://doi.org/10.1016/j.catcom.2019.105860 105860.

Nasir, A.M., Nordin, N.A.H.M., Goh, P.S., Ismail, A.F., 2018. Application of two-dimensional leaf-shaped zeolitic imidazolate framework (2D ZIF-L) as arsenite adsorbent: Kinetic, isotherm and mechanism. J. Mol. Liq. 250, 269–277. https://doi.org/10.1016/j.molliq.2017.12.005.

Oh, J.W., Cho, K.Y., Kan, M.Y., Yu, H.J., Kang, D.Y., Lee, J.S., 2020. High-flux mixed matrix membranes containing bimetallic zeolitic imidazole framework-8 for C_3H_6/C_3H_8 separation. J. Membr. Sci. 596,. https://doi.org/10.1016/j.memsci.2019.117735 117735.

Park, K.S., Ni, Z., Côté, A.P., Choi, J.Y., Huang, R., Uribe-Romo, F. J., Chae, H.K., O'Keeffe, M., Yaghi, O.M., 2006. Exceptional chemical and thermal stability of zeolitic imidazolate frameworks. Pnas 103, 10186–10191. https://doi.org/10.1073/pnas.0602439103.

Shiraishi, Y., Kofuji, Y., Sakamoto, H., Tanaka, S., Ichikawa, S., Hirai, T., 2015. Effects of surface defects on photocatalytic H_2O_2 production by mesoporous graphitic carbon nitride under visible light irradiation. ACS Catal. 5, 3058–3066. https://doi.org/10.1021/acscatal.5b00408.

Sharma, D., Kanchi, S., Sabela, M.I., Bisetty, K., 2016. Insight into the biosensing of graphene oxide: Present and future prospects. Arab. J. Chem. 9, 238–261. https://doi.org/10.1016/j.arabjc.2015.07.015.

Shi, L., Yang, L., Zhou, W., Liu, Y., Yin, L., Hai, X., Ye, J., 2018. Photoassisted construction of holey defective g-C_3N_4 photocatalysts for efficient visible-light-driven H_2O_2 production. Small 14, 1703142. https://doi.org/10.1002/smll.201703142.

Tiwari, S.K., Huczko, A., Oraon, R., Adhikari, A.D., Nayak, G.C., 2017. Facile electrochemical synthesis of few layered graphene from discharged battery electrode and its application for energy storage. Arab. J. Chem. 10, 556–565. https://doi.org/10.1016/j.arabjc.2015.08.016.

Vega, J., Andrio, A., Lemus, A.A., Díaz, J.A.I., Castillo, L.F., Gavara, R., Compañ, V., 2019. Modification of polyetherimide membranes with ZIFs fillers for CO_2 separation. Sep. Purif. Tech. 212, 474–482. https://doi.org/10.1016/j.seppur.2018.11.033.

Wu, Y., Chen, H., Liu, D., Qian, Y., Xi, H., 2015. Adsorption and separation of ethane/ethylene on ZIFs with various topologies: Combining GCMC simulation with the ideal adsorbed solution theory (IAST). Chem. Eng. Sci. 124, 144–153. https://doi.org/10.1016/j.ces.2014.07.019.

Wu, C., Liu, Q., Chen, R., Liu, J., Zhang, H., Li, R., Takahashi, K., Liu, P., Wang, J., 2017. Fabrication of ZIF-8@SiO_2 micro/nano hierarchical superhydrophobic surface on AZ31 magnesium alloy with impressive corrosion resistance and abrasion resistance. ACS Appl. Mater. Inter. 9, 11106–11115. https://doi.org/10.1021/acsami.6b16848.

Wang, R., Zhang, X., Li, F., Cao, D., Pu, M., Han, D., Yang, J., Xiang, X., 2018. Energy-level dependent H_2O_2 production on metal-free, carbon-content tunable carbon nitride photocatalysts. J. Energy Chem. 27, 343–350. https://doi.org/10.1016/j.jechem.2017.12.014.

Xu, P., Xu, H., Zheng, D., Ma, J., Hou, B., 2019. The reverse electrodialysis driven electrochemical process assisted by anodic photocatalysis for hydrogen peroxide production. Chemosphere 237,. https://doi.org/10.1016/j.chemosphere.2019.124509 124509.

Yang, J., Zhang, F., Lu, H., Hong, X., Jiang, H., Wu, Y., Li, Y., 2015. Hollow Zn/Co ZIF particles derived from core–shell ZIF-67@ZIF-8 as selective catalyst for the semi-hydrogenation of acetylene. Angew. Chem. Int. Edit. 54, 10889–10893. https://doi.org/10.1002/anie.201504242.

Yang, L., Dong, G., Jacobs, D.L., Wang, Y., Zang, L., Wang, C., 2017. Two-channel photocatalytic production of H_2O_2 over g-C_3N_4 nanosheets modified with perylene imides. J. Catal. 352, 274–281. https://doi.org/10.1016/j.jcat.2017.05.010.

Yang, S., Verdaguer-Casadevall, Arnau, Arnarson, L., Silvioli, Luca, Čolić, Viktor, Frydendal, R., Rossmeisl, J., Chorkendorff, I., Stephens, I.E.L., 2018. Toward the decentralized electrochemical production of H_2O_2: A focus on the catalysis. ACS Catal. 8, 4064–4081. https://doi.org/10.1021/acscatal.8b00217.

Yang, Y., Zeng, Z., Zeng, G., Huang, D., Xiao, R., Zhang, C., Zhou, C., Xiong, W., Wang, W., Cheng, M., Xue, W., Guo, H., Tang, X., He, D., 2019. Ti_3C_2 Mxene/porous g-C_3N_4 interfacial schottky junction for boosting spatial charge separation in photocatalytic H_2O_2 production. Appl. Catal. B-Environ. 258,. https://doi.org/10.1016/j.apcatb.2019.117956 117956.

Yang, H.C., Chao, M.W., Chou, C.J., Wang, K.H., Hu, C., 2020. Mushroom waste-derived g-C_3N_4 for methyl blue adsorption and cytotoxic test for Chinese hamster ovary cells. Mater. Chem. Phys. 244,. https://doi.org/10.1016/j.matchemphys.2020.122715 122715.

Zak, A.K., Majid, W.H.A., Abrishami, M.E., Yousefi, R., 2011. X-ray analysis of ZnO nanoparticles by Williamson-Hall and size–strain plot methods. Solid State Sci. 13, 251–256. https://doi.org/10.1016/j.solidstatesciences.2010.11.024.

Zhang, J., Zhang, T., Yu, D., Xiao, K., Hong, Y., 2015. Transition from ZIF-L-Co to ZIF-67: a new insight into the structural evolution of zeolitic imidazolate frameworks (ZIFs) in aqueous systems. CrystEngComm 17, 8212–8215. https://doi.org/10.1039/C5CE01531F.

Zaid, R.M., Chong, F.C., Teo, E.Y.L., Ng, E.P., Chong, K.F., 2015. Reduction of graphene oxide nanosheets by natural beta carotene and its potential use as supercapacitor electrode. Arab. J. Chem. 8, 560–569. https://doi.org/10.1016/j.arabjc.2014.11.036.

Zanon, A., Verpoort, F., 2017. Metals@ZIFs: Catalytic applications and size selective catalysis. Coordin. Chem. Rev. 353, 201–222. https://doi.org/10.1016/j.ccr.2017.09.030.

Zhang, H., Shi, X., Li, J., Kumar, P., Liu, B., 2019. Selective dye adsorption by zeolitic imidazolate framework-8 loaded UiO-66-NH_2. Nanomaterials 9, 1283. https://doi.org/10.3390/nano9091283.